Refining Power Converter Loss Evaluation: A Transfer Learning Approach

Ziheng Xiao, *Member, IEEE*, Yu Jiang, *Member, IEEE*, Tengfei Sun, *Graduate Student Member, IEEE*, Yue Wu, *Graduate Student Member, IEEE*, and Yi Tang, *Senior Member, IEEE*

***Abstract*—A precise evaluation of power converter losses is essential for accurately predicting power loss and optimizing control parameters to enhance efficiency across various scenarios and applications. Conventional power loss evaluation methods separate the theoretical analysis and experimental verification stages. Consequently, these methods often suffer from irreconcilable disparities between the analytical predictions and measurement outcomes. This article introduces a transfer learning (TL)-based refinement approach for power loss evaluation, which can be iteratively improved with ongoing experimental data. Our method entails the creation of an extensive source domain dataset for training a source domain model, followed by fine-tuning in the target domain. Consequently, a self-adaptive and refined power loss evaluation model is established with a small amount of experimental data. We conducted a case study featuring a 6.6 kW synchronous boost converter, considering six degrees of freedom for operational conditions. Leveraging a dataset of 2 33 280 simulation samples and 45 experimental samples, our refined power loss evaluation model achieved a remarkable 50% reduction in average power loss error compared with conventional methodologies. Guided by the TL refined power loss model, the peak efficiency and corresponding optimal control parameters can be obtained.**

***Index Terms*—Artificial intelligence, power loss evaluation, transfer learning (TL).**

I. Introduction

POWER electronics plays a dominant role in the processing of electrical energy. In total, 70% of electrical energy today is processed by power electronics, and this will increase in the coming decades [1]. Power converters stand as the fundamental equipment in a wide range of applications, including renewable energy systems [2], [3], [4], electrified transportation [5], [6], [7], smart grids [8], [9], [10], and modern data centers [11], [12], [13].

Manuscript received 16 September 2023; revised 22 November 2023; accepted 27 December 2023. Date of publication 2 January 2024; date of current version 16 February 2024. Recommended for publication by Associate Editor S. Mazumder. *(Corresponding author: Yi Tang.)*

Ziheng Xiao and Tengfei Sun are with the Energy Research Institute, Nanyang Technological University, Singapore 639798 (e-mail: ziheng.xiao@ntu.edu.sg; tengfei.sun@ntu.edu.sg).

Yu Jiang is with the School of Electrical Engineering, Chinese University of Hong Kong, 999077, Hong Kong (e-mail: yujiang@cuhk.edu.hk).

Yue Wu is with the School of Electrical Engineering, Xi'an Jiaotong University, Xi'an 710049, China (e-mail: dywuyue@stu.xjtu.edu.cn).

Yi Tang is with the School of Electrical and Electronic Engineering, Nanyang Technological University, Singapore 639798 (e-mail: yitang@ntu.edu.sg).

Color versions of one or more figures in this article are available at https://doi.org/10.1109/TPEL.2023.3349178.

Digital Object Identifier 10.1109/TPEL.2023.3349178

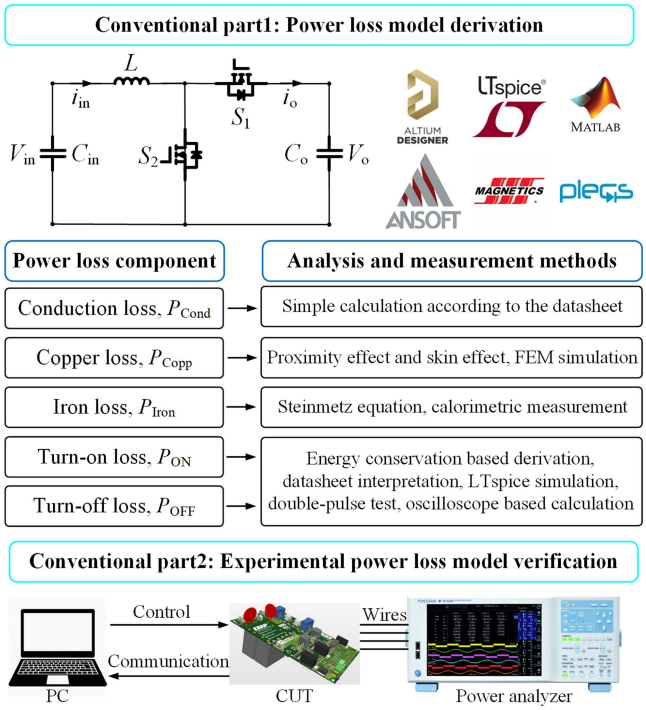

Fig. 1. Derivation and verification processes of the conventional power loss model.

In applications like battery chargers for electric vehicles and the dc–dc stage in solar systems, where voltage and power exhibit wide-ranging variations, achieving high efficiency is not just essential during rated operating conditions, but also in light load, high step-up ratio, or high step-down ratio conditions. The precision in assessing power loss becomes paramount in these applications to ensure accuracy across a broad spectrum of operational conditions. This significance amplifies when managing multiple adjustable control parameters, including switching frequency, duty ratios, deadtime, modulation schemes, etc. The accuracy of the power loss evaluation model directly impacts the credibility with which "optimal control parameters" can be selected to minimize power loss. The process of conducting exhaustive power loss measurements and searching for optimal control parameters using a power analyzer can be both laborious and time-consuming across various operating conditions.

The derivation and verification processes of the conventional power loss model are illustrated in Fig. 1, typically segmented

into two distinct parts. In the first part, the power loss model is derived. For specific power electronics topologies, such as a synchronous boost converter, the total power loss can be assessed through either formula-based power loss calculation or simulation-based power loss simulation, contingent on the characteristic of the power loss component.

The overall power loss, P_{Loss}, can be classified into the conduction loss, P_{Cond}, the copper loss, P_{Copp}, the iron loss, P_{Iron}, the turn-ON loss, P_{ON}, and the turn-OFF loss, P_{OFF} [14]. P_{Cond} is relatively straightforward once the root-mean-square (RMS) values of all resistive components in the converter under test (CUT) are known. P_{Copp}, also referred to as ac winding loss, is associated with proximity and skin effects [15]. The eddy current losses caused by these effects can be analytically calculated or simulated using software based on the finite-element method [16]. P_{Iron} is typically calculated using the Steinmetz equation or its improved versions [17], [18], [19]. Calorimetric-based measurements are commonly employed to accurately determine P_{Iron}, encompassing both steady-state and transient measurements [20], [21]. The derivation process of P_{ON} and P_{OFF} can be challenging due to the voltage-dependent nature of parasitic capacitors, as key parameters may be unknown [22]. To overcome this challenge, two methods are commonly used. The first method involves interpreting datasheets to obtain a simple and fast calculation. While this method is convenient, it may not account for all the parasitic components in the actual circuit. The second method involves using LTspice simulation, which offers a more accurate approach. During the measurement phase, the widely adopted technique is the double pulse test (DPT) [23], [24]. An oscilloscope is employed to measure the switching data. These data are saved for further data analysis and postprocessing to evaluate P_{ON} and P_{OFF} accurately.

Once established, this power loss model remains unchanged, allowing the use of a power analyzer to measure the actual power loss of a CUT in part 2, which shares identical electrical parameters. Since the theoretical analysis part and the experimental verification part are conducted independently, lacking communication or feedback between them. As a result, any discrepancies between these two parts remain irreconcilable.

This raises a fundamental question: Is it possible to refine or enhance the power loss evaluation model based on the insights gleaned from experimental data? This aspect holds paramount significance, as refining our model could potentially mitigate the disparities between theoretical analysis and experimentation as more data is acquired.

Guided by this concept, this article endeavors to ascertain a refined approach to power converter loss evaluation by amalgamating simulation and experimental data, subsequently incorporating a transfer learning (TL) methodology. TL emerges as a suitable approach with the potential to overcome the gap. TL is a technique within the realm of artificial intelligence (AI) that harnesses knowledge acquired from solving one problem to aid in solving a different yet related problem [25]. This technique involves pretraining a model on a large dataset from a source task and subsequently fine-tuning it on a smaller dataset from a target task. TL has found extensive applications across diverse domains, including image classification (e.g., ResNet [26]), object detection (e.g., YOLO [27]), natural language processing (e.g., OpenAI's GPT [28] and Google's BERT [29]), etc.

The proposed TL-based power converter loss evaluation refinement method involves creating a dataset in the source domain using an iterative simulation and calculation process. An artificial neural network (ANN) is employed to learn the power loss of the power converter across various operating conditions. Once the ANN model is trained in the source domain and has acquired knowledge, this knowledge can be transferred to the target domain using a TL approach. Consequently, a power loss evaluation model, capable of refinement, can be established with a minimal amount of experimental data. This model is data-driven and self-adaptive, enabling its accuracy to be continuously enhanced through iterative updates using ongoing experimental data. After obtaining the TL refined power loss model, we can iteratively apply this model to search for optimal control parameters across various operational conditions.

The rest of this article is organized as follows. Section II introduces the proposed solution for the power loss evaluation refinement. In Section III, the process of acquiring the source data, training the ANN in the source domain, and implementing TL in the target domain ANN is outlined. Section IV presents the experimental results, and finally, Section V concludes this article by summarizing the findings.

II. Proposed Power Loss Evaluation Refinement

Fig. 2 illustrates the flowchart detailing the refinement process for evaluating power loss in the proposed approach. In this article, the analysis part is denoted as the "Source Domain." The data in source domain is "Cheap," which indicates that it is relatively easy to obtain a large amount of data according to the formulas, datasheets, and iterative simulation results. By applying the converter's fundamental operating principle, various types of power losses can be derived, calculated, and simulated in the analysis part. In contrast, the experimental verification part is referred to as the "Target Domain," and it involves a distinct approach. In the case of an assembled CUT, a commonly employed method is to assess its power loss using a power analyzer. A personal computer (PC) is connected to the CUT to transmit operational commands.

To ensure safe operation of the CUT, an oscilloscope is utilized to measure critical electrical parameters throughout the testing process. The real-time waveforms, along with the measured power loss, are recorded and stored in .PNG or .CSV file formats for further analysis and breakdown of power losses. This process is time-consuming and tedious. To evaluate the performance of the CUT under various conditions such as voltage, power, switching frequency, and modulation schemes, manual adjustments are necessary. These include configuring the output voltage of the dc power supply, setting the resistance of the dc load bank, and sending operation commands from the PC. Through source domain training and target domain TL, the power loss ANN model for the CUT can be obtained. This model is inherently self-adaptive, with its accuracy continuously improving as additional experimental data becomes available.

By amalgamating the features of TL and the power loss evaluation methods, the process of the proposed power loss evaluation

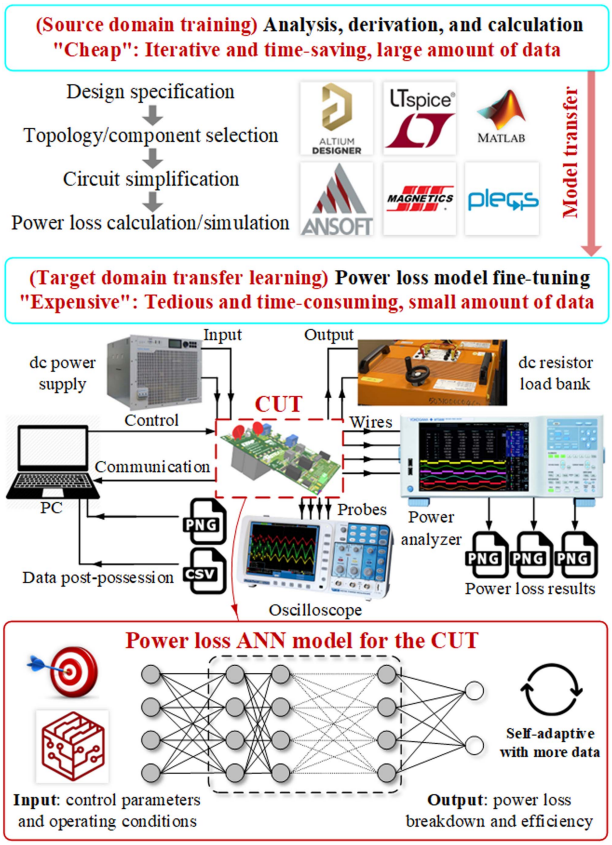

Fig. 2. Flowchart detailing the refinement process for evaluating power loss in the proposed approach.

refinement is illustrated in Fig. 3. The flowchart comprises the following three principal stages.

1) Data generation in the source domain.
2) ANN training in the source domain.
3) ANN fine-tuning in the target domain.

It is essential to highlight that, during the power loss data acquisition processes in both the source domain (simulation) and target domain (experiment), the heat factor is not taken into consideration for the following reasons.

1) In the simulation process, assuming a constant temperature of 25 °C requires approximately two weeks to gather sufficient data. Introducing considerations for heat significantly extends the duration of data acquisition in the source domain.
2) In experiments conducted at a room temperature of 25 °C, various components, such as power MOSFETs and power inductors, exhibit diverse temperatures at different times. Consequently, obtaining precise heat data for all components becomes challenging.
3) The power loss data from experiments lacks labels. The power analyzer only provides the total power loss P_{Loss}, and ground truth data is absent for individual components like P_{Cond}, P_{Copp}, P_{Iron}, P_{ON}, and P_{OFF} for each experimental sample.

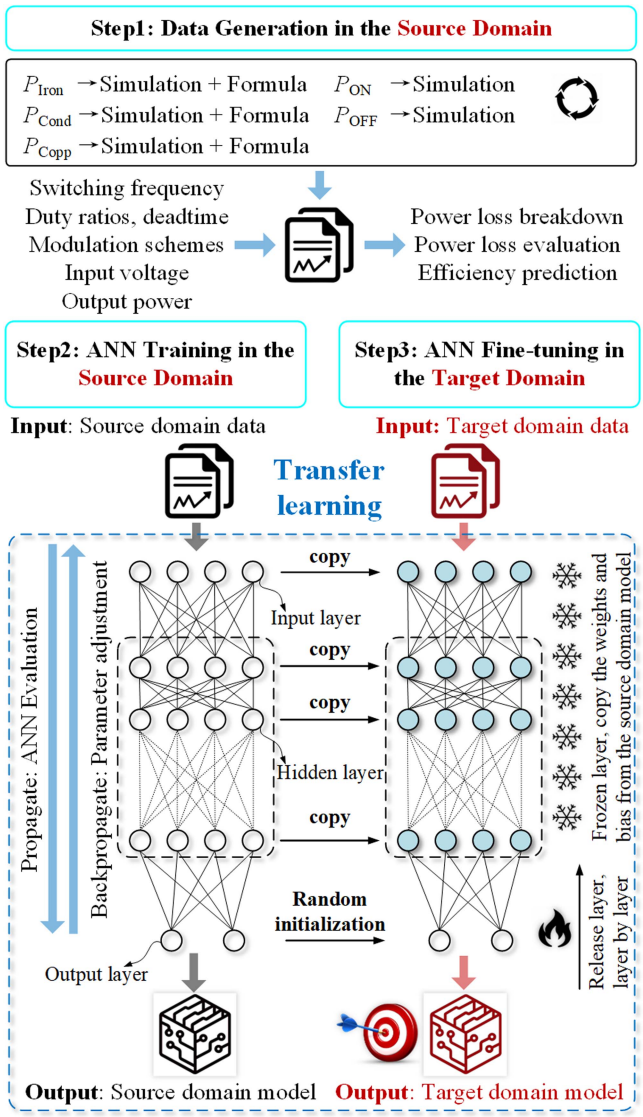

Fig. 3. Flowchart diagram of the proposed TL-based power loss evaluation refinement of power converters.

A. Data Generation in the Source Domain

In Step1, different parts of power losses are determined using a combination of simulation and formula-based methods. These calculations are carried out iteratively to generate a dataset in the source domain. The input variables of the iterations include the following: switching frequency f_{s}, the duty ratios of the power MOSFETs, the deadtime T_{d}, the modulation schemes, the input voltage V_{in}, and the output power P_{o}.

Considering the distinctive characteristics of different aspects of power losses, namely P_{Cond}, P_{Copp}, and P_{Iron}, these are typically derived through simulations alongside corresponding formulas, while P_{ON} and P_{OFF} are primarily acquired via simulation exclusively. The outcome variables resulting from these iterative processes encompass power loss breakdown, power loss assessment, and efficiency prediction. However, achieving a detailed power loss breakdown during the experimental verification phase is challenging, given the absence of ground

truth values for these components. In the quest for enhanced power loss evaluation, the individual power loss components are cumulatively summed to calculate the overall power loss. Subsequently, the experimental measurements can be employed to refine the power converter loss evaluation methodology.

B. ANN Training in the Source Domain

In Step2, a feedforward ANN is selected to learn the intrinsic relationships within the dataset from the source domain. The training process involves both forward propagation and backpropagation. Following forward propagation, a comparison is made between the predicted output of the network and the actual target output. The error or loss between these values is computed. Backpropagation is then initiated to propagate this error backward through the network, enabling the adjustment of weights and biases to minimize the error. This iterative process of forward and backward propagation continues until the error falls below a predefined threshold. At this point, the source domain model is obtained, and the source domain model has effectively learned the underlying patterns within the dataset.

C. ANN Fine-Tuning in the Target Domain

The process of fine-tuning in TL involves adapting the source domain model to the target domain using a smaller dataset. In Step3, the weights and biases in each layer of the source domain model are directly copied to the corresponding layers of the target domain model. By freezing specific layers, we retain the pretrained knowledge captured by those layers. Typically, layers closer to the input capture more general features, while layers closer to the output are task-specific and should be fine-tuned with the new data.

This process proves beneficial when the data for the target domain is limited. Freezing layers helps prevent overfitting and facilitates faster convergence of the target domain model. Striking a balance is crucial between the number of layers frozen and the number of layers fine-tuned. Freezing too many layers may limit the model's adaptability in the target domain, while fine-tuning too many layers may lead to overfitting.

As the source domain model and the target domain model address the same task, only the output layer is released and randomly initialized at the very beginning. Hyperparameters such as the learning rate, batch size, and number of training epochs for the training strategy are adjusted empirically. The frozen layers are subsequently released layer by layer, starting from the output layer and moving toward the input layer, during multiple training processes. Experimentation and validation on a separate dataset are crucial to determining the optimal configuration for freezing layers in this process.

III. Case Study of a Synchronous Boost Converter

This section provides a case study on a 6.6 kW synchronous boost converter. It is important to note that this article does not delve into an exhaustive design optimization process. Fig. 4 presents typical waveforms, and Table I summarizes key parameters. In this example, the duty ratios of S_1 and S_2 are represented as D_1 and D_2, respectively. Both the continuous current modulation (CCM), and the triangular current modulation (TCM) are investigated. In the case of TCM, both S_1 and S_2 are switched OFF when the inductor current, denoted as $i_{\rm L}$, reaches zero. The freewheeling period lasts for 1–D_1–D_2. Additionally, the turn-ON and turn-OFF currents for S_1 and S_2 are denoted as $i_{\rm S1\_1}$, $i_{\rm S1\_2}$ and $i_{\rm S2\_1}$, $i_{\rm S2\_2}$, respectively.

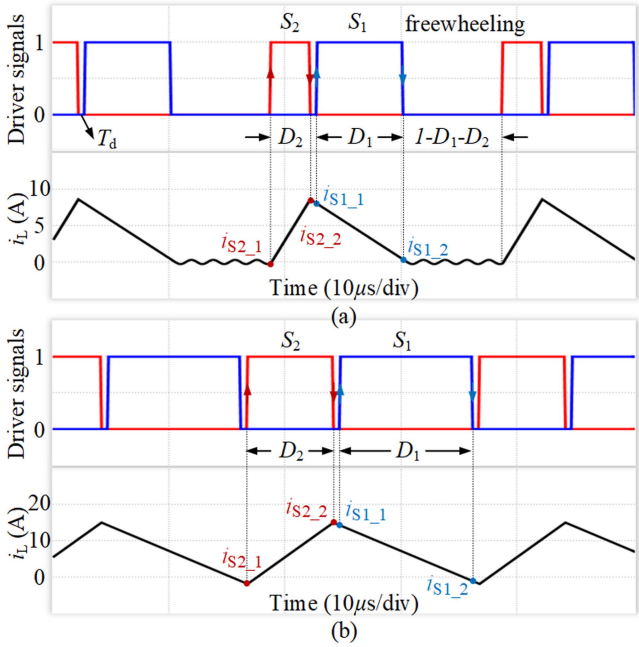

Fig. 4. Typical waveforms of a synchronous boost converter in different modulation schemes. (a) TCM. (b) CCM.

TABLE I
Key Parameters of the Synchronous Boost Converter

Key parameters	Values
Input voltage (V)	200 – 600
Output voltage (V)	450 – 800
Maximum output power (kW)	6.6
Switching frequency (kHz)	25 – 100
Range of D_1 (p.u.)	0.55 – 1.00
Range of D_2 (p.u.)	0 – 1- D_1
Deadtime (ns)	200 – 600
Inductance (μH)	526

A. Step1.1: Source Data Generation of Iron Loss, Conduction Loss, and Copper Loss

The process of generating source data for $P_{\rm Iron}$, $P_{\rm Cond}$, and $P_{\rm Copp}$ is illustrated in Fig. 5. Initially, we employ a formula-based calculation to determine the dc bias of the chosen high-flux core for the inductor.

Assuming the synchronous boost converter to be a lossless system, the equation for the inductor current ripple, denoted as $i_{\rm L\_AC}$, can be expressed as follows:

$$i_{\rm L\_AC} = \frac{V_{\rm in} D_2}{f_{\rm s} L} = \frac{(V_{\rm o} - V_{\rm in})\, D_1}{f_{\rm s} L}. \tag{1}$$

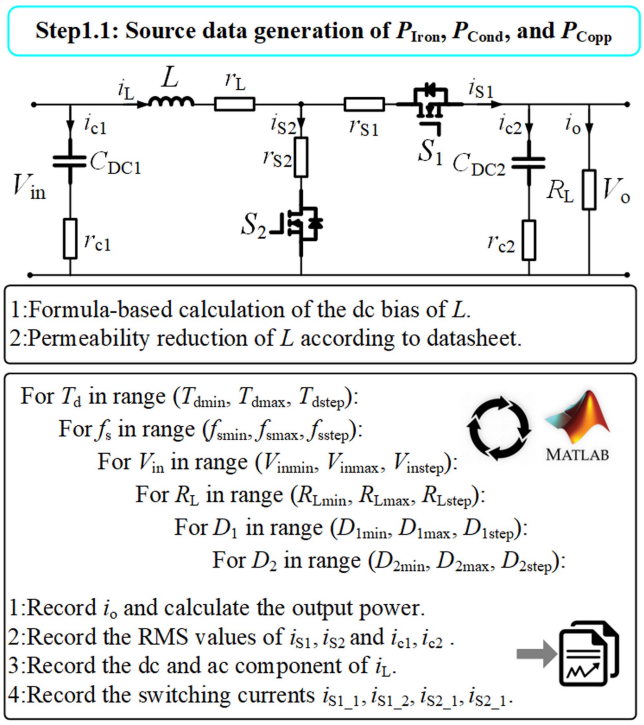

Fig. 5. Flowchart of the source data generation of P_{Iron}, P_{Cond}, and P_{Copp}.

The voltage gain of the synchronous boost converter M is given as follows:

$$M = \frac{V_o}{V_{in}} = \frac{D_1 + D_2}{D_1}. \tag{2}$$

According to the power conservation law, the dc component of the inductor current, i_{L_DC} is given as follows:

$$V_{in} i_{L-DC} = V_o i_{o\_DC} = P_o \Rightarrow i_{L-DC} = \frac{P_o}{V_{in}}. \tag{3}$$

In TCM, i_{L_DC} is half of the peak inductor current, and the following equations are given as follows:

$$\frac{V_{in} D_2}{L} = \frac{(V_o - V_{in}) D_1}{L} = \frac{i_{L-DC}}{2} \Rightarrow \begin{cases} D_1 = \frac{1}{M-1} \frac{2LP_o}{V_{in}^2} \\ D_2 = \frac{2LP_o}{V_{in}^2} \end{cases}. \tag{4}$$

Because $D_1 + D_2$ should be smaller than unity, the maximum output power in TCM is given as follows:

$$P_o < \frac{(M-1) V_{in}^2}{2ML}. \tag{5}$$

In both CCM and TCM, the dc bias magnetic field strength, H_{dc} is calculated as follows:

$$H_{dc} = \frac{N i_{L-DC}}{l_e} = \frac{N P_o}{V_{in} l_e} \tag{6}$$

where N denotes the turns of winding while l_e denotes the magnetic core length.

H_{dc} introduces a permeability reduction, and the reduction rate given from the core datasheet is as follows:

$$\frac{\mu_r (H_{dc})}{\mu_r (0)} = \frac{1}{a_1 + a_2 H_{dc}^{a_3}} \tag{7}$$

TABLE II
COMPONENTS AND KEY ELECTRICAL PARAMETERS OF THE CUT

Component	Part number	Parameters
MOSFETs	IMZA120R020M1H	1200 V, 19 mΩ, 4.2 V v_{Th}
MCU	TMS320F28377D	Digital signal processer C2000 32-bit 200-MHz
Input capacitor	C4AQIBW5150B3FJ	15 μF, 800 V film cap, 10 nH ESL, 4.7 mΩ ESR
Output capacitor	MKP1848C61012JP4	20 μF, 1.2 kV film-cap, 18 nH ESL, 8 mΩ ESR
Inductor cores	Magnetics high flux 060 core, C058439	4 cores in parallel, 526 μH @50 kHz
Inductor wires	14 AWG hook-up wire	31 turns, 57 mΩ resistance
Core parameters		l_e = 107 mm, V_e = 21,300 mm^3, a_1 = 0.01, a_2 = 2.582E-07, a_3 = 2.166, a_4 = 8.049E-02, a_5 = 1.887E-02, a_6 = 9.733E-04, a_7 = 7.198E-02, a_8 = 6.927E-04, a_9 = 1.660, k = 47.51, α = 1.585, β = 1.43
Wires parameters		σ = 120.77 m/Ω, d_r = 1.715 mm.

where a_1, a_2, and a_3 are the material parameters.

The inductance of the power inductor with V_{in} and P_o can be calculated as follows:

$$L(P_o, V_{in}) = \left(a_1 + a_2 \left(\frac{N P_o}{V_{in} l_e}\right)^{a_3}\right)^{-1} L(0,0). \tag{8}$$

Table II provides a summary of the key electrical parameters associated with the synchronous boost converter circuit. The inductance L, and winding resistance r_L of the power inductor are measured using an impedance analyzer. The drain-source on-state resistance $r_{ds\text{-}ON}$ of the two power MOSFETs, as well as the equivalent series resistance (ESR) of the two film capacitors, r_{c1} and r_{c2}, are extracted from their datasheets, respectively.

The circuit is subjected to iterative simulations comprising six loops. The variables within each loop include the deadtime T_d, switching frequency f_s, input voltage V_{in}, load resistor R_L, and duty ratios D_1, D_2. During each iteration, a simulation duration of 50 ms is employed to ensure that the circuit reaches a steady state. The time step is set to 1E-7, providing ample resolution even at high switching frequencies. Data recorded between 49 and 50 ms is saved for analysis. Various parameters are calculated using 10 000 samples averaged over the duration, including the output current i_o, the RMS values of i_{S1}, i_{S2}, and i_{c1}, i_{c2}, as well as the dc and ac components of i_L. Additionally, the four switching currents, i_{S1_1}, i_{S1_2}, i_{S2_1}, and i_{S2_2}, are recorded based on their values during the first switching cycle after 49 ms. In the case of TCM, the diode conduction loss is neglected during the freewheeling period since the inductor current is minimal in this condition.

Based on the simulation data obtained during the iterations, the maximum and minimum magnetic field strengths, denoted as H_{max} and H_{min}, respectively, can be determined as follows:

$$\begin{cases} H_{Max} = \frac{N(2i_{L-DC} + i_{L-AC})}{2l_e} \\ H_{Min} = \frac{N(2i_{L-DC} - i_{L-AC})}{2l_e} \end{cases}. \tag{9}$$

The corresponding maximum and minimum flux densities, denoted as B_{max} and B_{min}, respectively, can be calculated using

TABLE III
KEY PARAMETERS OF THE DRIVER CIRCUITS

Component	Parameters
Driver IC	1ED3461MU12MXUMA1 from Infineon 9 A peak current, 5.7 kV isolated voltage
Driver source	QA123C-1504R3 from Mornsun +15 V/–4 V outputs, 120 mA output current
Turn-ON resistor	Both RC2512FK-0720RL from YAGEO, 20 Ω, 1% tolerance, two in parallel
Turn-ON resistor	
Power loop inductance	L_{p1} = 7.2 nH, L_{p2} = 2.4 nH, L_{p3} = 3.1 nH, L_{p4} = 5.9 nH, L_{dc} = 18 nH
Driver loop inductance	$L_{loop\text{-}dr}$ = 8.4 nH

the fitted formula derived from the datasheet with

$$B(H) = \left(\frac{a_4 + a_5 H + a_6 H^2}{1 + a_7 H + a_8 H^2}\right)^{a_9} \tag{10}$$

where a_4–a_9 are the material parameters.

The ac component of the flux density, B_{AC} is given as follows:

$$B_{AC} = \frac{B(H_{Max}) - B(H_{Min})}{2}. \tag{11}$$

Consequently, P_{Iron} can be calculated as follows:

$$P_{Iron} = k f_s^{\alpha} B_{AC}^{\beta} V_e \tag{12}$$

where k, α, and β are the Steinmetz coefficients of the material, and V_e is the effective volume of the core.

The wires utilized in the inductor are categorized as round conductors. The copper losses caused by both the skin effect and proximity effect can be analytically calculated using modified Bessel functions. The skin effect induced, and proximity effect induced losses, denoted as P_{Skin} and P_{Prox}, can be simplified as follows:

$$\begin{cases} P_{Skin} \approx \frac{2}{\pi \sigma d_r^2} i_{L\_AC}^2 \\ P_{Prox} \approx \frac{\pi \sigma^2 f_s^2 d_r^2}{32} i_{L\_AC}^2 \end{cases} \tag{13}$$

where σ is the material conductivity and d_r is the diameter of the wires. To summarize, the input variables for this dataset are (V_{in}, R_L, D_1, D_2, T_d, f_s), while the output variables include (i_{S1_1}, i_{S1_2}, i_{S2_1}, i_{S2_2}, P_{Iron}, P_{Cond}, P_{Copp}).

B. Step1.2: Source Data Generation of Turn-on Loss, and Turn-off Loss

The process of generating source data for turn-ON loss E_{ON} and turn-OFF loss E_{OFF} is depicted in Fig. 6. First, the printed circuit board (PCB) designed in Altium Designer is exported for analysis in AnsoftLinks, where the parasitic parameters of the PCB traces, vias, and copper pours are extracted. Among these, the key parasitic components include the power loop parasitic inductances L_{p1}–L_{p4} and the driver loop parasitic inductance $L_{loop\text{-}dr}$. Table III provides a summary of the key parameters for the power MOSFET half-bridge DPT configuration and their corresponding driver circuits. Considering the circuit layout and the parasitic components present in the PCB, the DPT circuit is simulated in LTspice. The simulation incorporates models of the driver integrated circuit (IC) and power MOSFETs obtained from the manufacturer. Notably, the power $_{mosfets}$ model encompasses

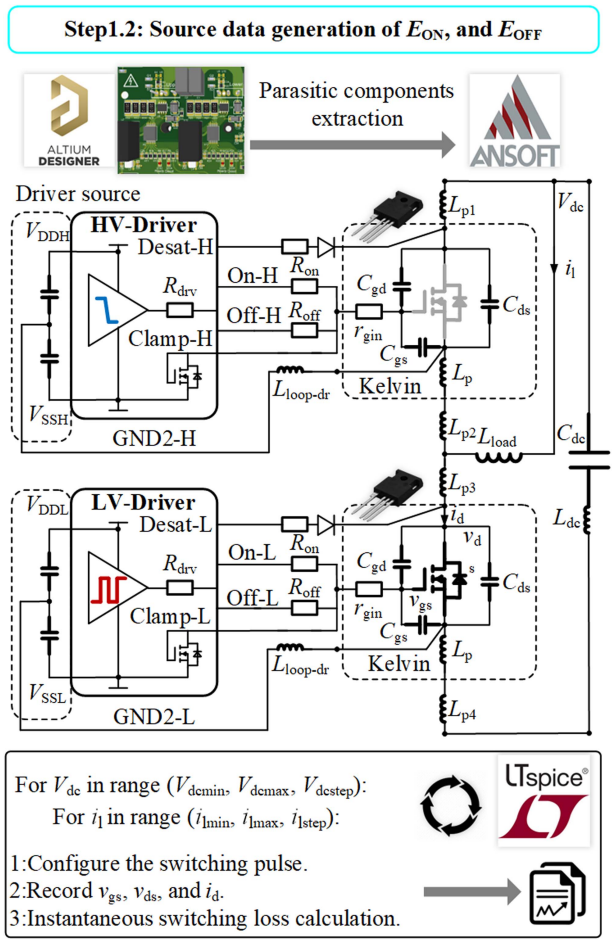

Fig. 6. Flowchart of the source data generation of E_{ON} and E_{OFF}.

information regarding nonlinear parasitic capacitors and the parasitic inductance.

Regarding the designed PCB circuit and layout, all electrical components remain fixed during the simulation, while the iteration variables are the dc voltage V_{dc}, and the load inductor i_l. Throughout the simulation, a time step of 1E-9 is utilized. In each DPT simulation, the duration of the switching pulse is calculated to ensure that the desired switching currents can be obtained. Once a DPT simulation is completed, information such as gate-source voltage $v_{gs}(V_{dc}, i_l, t)$, drain-source voltage $v_{ds}(V_{dc}, i_l, t)$, and drain current $i_d(V_{dc}, i_l, t)$ is saved. The values of E_{ON} and E_{OFF} are then determined by integrating the product of $v_{ds}(V_{dc}, i_l, t)$ and $i_d(V_{dc}, i_l, t)$.

To summarize, the input variables for this dataset are (V_{dc}, i_l), while the output variables are (E_{ON}, E_{OFF}). It is important to note that Step1.2 is specifically employed to establish the relationship between switching losses under different voltage and current conditions. Therefore, this process is repeated four times to calculate the values of P_{ON} and P_{OFF} for the power MOSFETs across the four switching currents (i_{S1_1}, i_{S1_2}, i_{S2_1}, i_{S2_2}) with switching frequency f_s. It should be emphasized that when i_{S2_1} is less than zero, zero voltage switching-ON (ZVS-ON) is achieved and the corresponding E_{ON} is considered as zero.

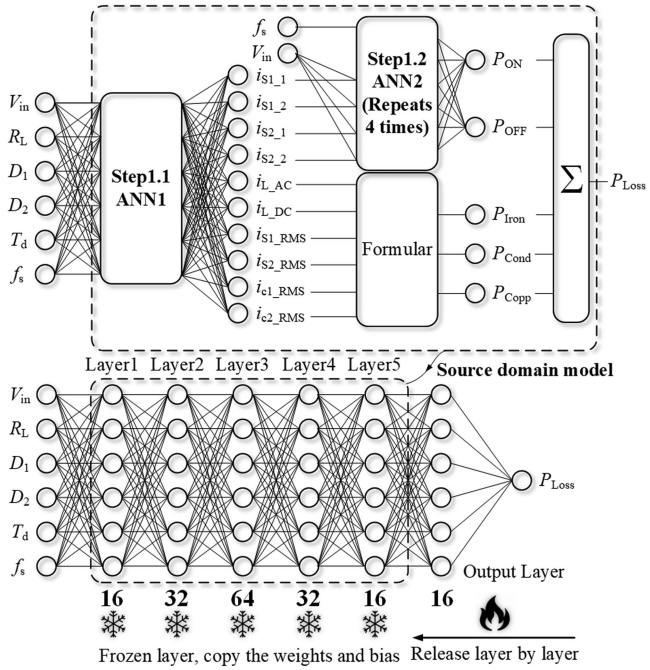

Fig. 7. Process of obtaining and training the source domain model and the TL process.

TABLE IV
KEY VARIABLES IN ANN1 AND ANN2

Item	Values
(V_{inmin}, V_{inmax}, V_{instep})	(100, 600, 100) V
(R_{Lmin}, R_{Lmax}, R_{Lstep})	(100, 450, 50) Ω
($D_{1\text{min}}$, $D_{1\text{max}}$, $D_{1\text{step}}$)	(0.55, 0.95, 0.05) p.u.
($D_{2\text{min}}$, $D_{2\text{max}}$, $D_{2\text{step}}$)	(0.05, 1-D_1, 0.05) p.u.
(T_{dmin}, T_{dmax}, T_{dstep})	(200, 600, 200) ns
(f_{smin}, f_{smax}, f_{sstep})	(25, 100, 25) kHz
(V_{dcmin}, V_{dcmax}, V_{dcstep})	(150, 850, 25) V
(i_{lmin}, i_{lmax}, i_{lstep})	(1, 40, 1) A

C. ANN Structure of the Source Domain Model

By integrating the two steps, we present the diagram of the source domain model in Fig. 7. This model consists of two ANNs corresponding to the two steps. The initial values, end values, and iteration steps of all variables in ANN1 and ANN2 are summarized in Table IV. Consequently, ANN1 and ANN2 comprise $6\times8\times9\times45\times4\times3 = 233280$ and $71\times40 = 2840$ samples, respectively. To ensure that the source and target domains share the same ANN structure, all power losses are aggregated, resulting in a dataset with 6 inputs and 1 output for the source domain. The size of the source domain dataset is also 2 33 280, matching the number of samples in ANN1.

The source domain model employs a five hidden layer ANN architecture, with neuron configurations of 16, 32, 64, 32, and 16 in each respective hidden layer. These configurations are first determined through an empirical design approach and then tested for a multiple time via trial-and-error method. The inputs to the ANN consist of (V_{in}, R_{L}, D_1, D_2, T_{d}, f_{s}), while the output variable is P_{Loss}. To prepare the data for training, the original dataset is shuffled, and then divided into three sets: a 70% training set, a 20% testing set, and a 10% validation set.

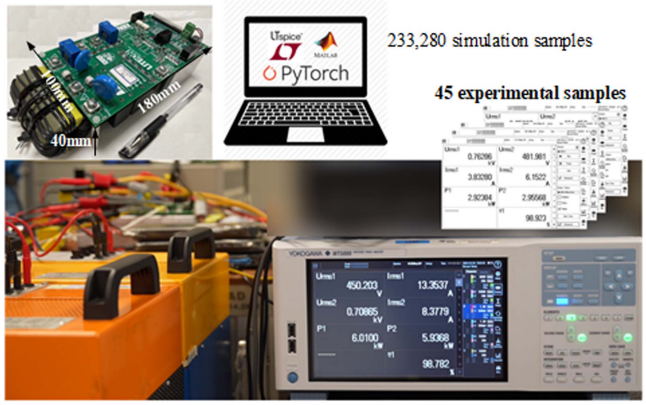

Fig. 8. Power loss measurement platform of the 6.6 kW synchronous boost converter.

The Adam optimizer is utilized, with an initial learning rate of 0.01.

The training process is performed for a total of 2000 epochs, and the learning rate is reduced to 1/10 every 500 epochs. The model is trained using the PyTorch framework, and the trained model achieves a mean absolute percentage error (MAPE) of 4.06%. The MAPE for m samples is calculated using the following equation, where $\hat{Y}_{\text{i}}$ represents the predicted output and Y_{i} represents the actual output of the ith sample.

$$\text{MAPE} = \frac{100\%}{m}\sum_{i=1}^{m}\left\|\frac{\hat{Y}_i - Y_i}{Y_i}\right\|. \tag{14}$$

A lower MAPE value indicates a more accurate and reliable model.

IV. EXPERIMENTAL VERIFICATION

The experimental verification is conducted using a 6.6 kW synchronous boost converter, as depicted in Fig. 8. The physical dimension of the prototype is $100\times180\times40$ mm^3. The key parameters are summarized in Tables I–III. A total of 45 experimental samples are obtained, capturing various combinations of V_{in}, R_{L}, D_1, D_2, T_{d}, and f_{s}. The comprehensive parameters of these experimental samples are encapsulated in Fig. 9. The distribution of the experimental samplings encompasses a relatively broad spectrum of (V_{in}, R_{L}, D_1, D_2, T_{d}, f_{s}) to ensure robust refinement. The testing ambient temperature is 25 °C. The measurement of power loss was carried out using the Yokogawa WT5000 power analyzer (18-bit resolution). Cooling of the heatsink and power inductor of the synchronous boost converter is facilitated by a 12 V, 3 W dc fan with an airflow of 4.1 cubic feet per minute. Efficiency recordings of the converter are taken once it reaches a steady state, preventing a substantial temperature increase in each electrical component.

A. Power Loss Evaluation Model Derivation

We have employed two distinct methods for power loss evaluation. In Method1 (conventional power loss calculation method), we utilize a formula-based and datasheet-based approach where P_{Iron}, P_{Cond}, and P_{Copp} are computed using relevant formulas,

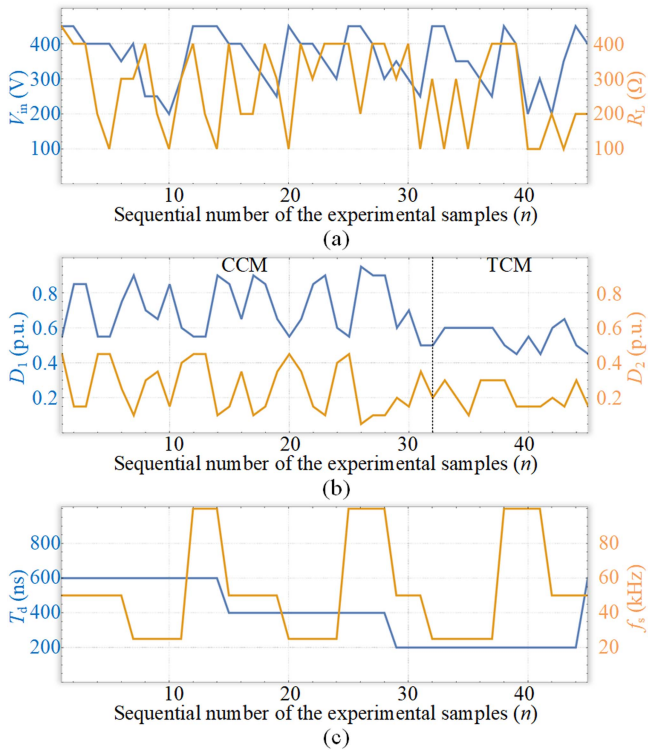

Fig. 9. Parameters encompassing six degrees of freedom across the 45 experimental samples. (a) Input voltage V_{in} and load resistance R_{L}. (b) Duty ratios D_1 and D_2. (c) Deadtime T_{d} and switching frequency f_{s}.

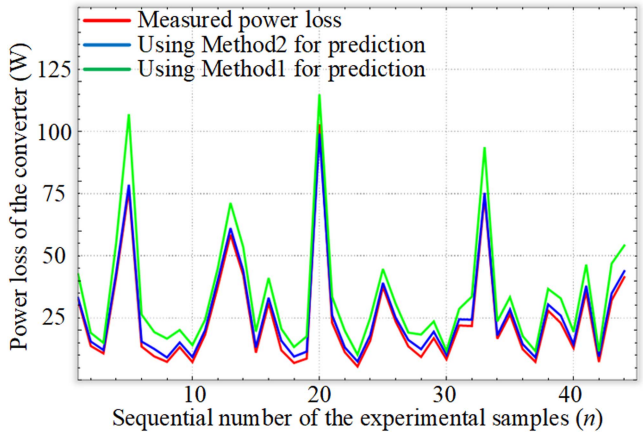

Fig. 10. Measured power losses from the 45 experimental samples and the corresponding predicted power losses obtained through both methods.

while P_{ON} and P_{OFF} are inferred from datasheets. Meanwhile, Method2 adopts a more comprehensive power loss evaluation approach, as exemplified in the case study. Here, P_{Iron}, P_{Cond}, P_{Copp}, P_{ON}, and P_{OFF} are derived through iterative simulations and the application of suitable formulas.

Fig. 10 presents both the measured power losses from the 45 experimental samples and the corresponding predicted power losses obtained through both methods. A comprehensive comparison of these two evaluation methods is provided in Table V. Notably, when opting for the more comprehensive power loss evaluation method (Method2), the primary time consumption

TABLE V
COMPARISON OF THE TWO EVALUATION METHODS

Comparison item	Method1	Method2
Average MAPE of power loss prediction	17.3%	**10.1%**
Maximum MAPE of power loss prediction	106.4%	**37.1%**
Minimum MAPE of power loss prediction	6.73%	**1.75%**
Time consumption in the data collection stage	15 s*	**14.5 days**
Time consumption in the ANN training stage	**Around 3 h**†	
Time consumption in the TL fine-tuning stage	**Around 4 min**†	
Time consumption in one power loss prediction	**Around 3 ms**†	

*Time consumption of an analytical method to generate 233,280 samples.
†Based on Intel(R) Core(TM) i7-3770 CPU and 8GB RAM. It can be reduced to around 3 days if we replace the CPU to Intel(R) Core(TM) i9-12900K.

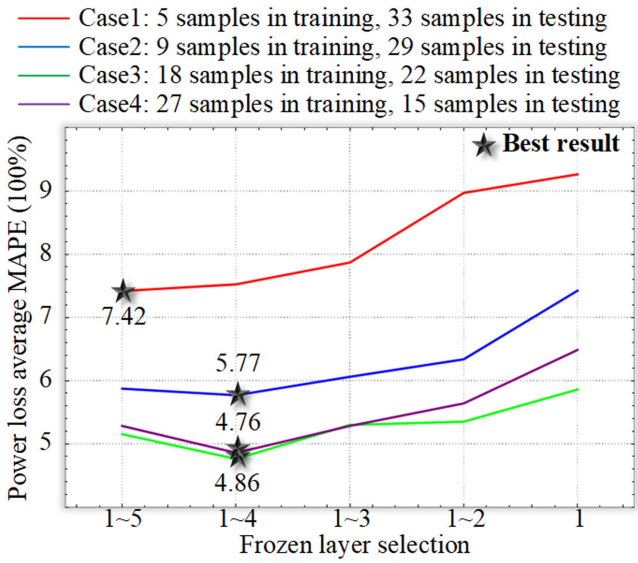

Fig. 11. Average MAPE of the power losses predicted by the target domain model by freezing different hidden layers in four different cases.

arises from the iterative simulation during the data generation stage.

As the TL fine-tuning stage is exceptionally rapid, the refined model can be readily updated with continuous experimental data. During the TL refinement process based on Method2, the 45 samples are divided into training, testing, and validation sets. In this process, the percentage of the testing set is increased, and we choose different ratios for the three sets: Case1: (10:72:18), Case2: (20:64:16), Case3: (40:48:12), and Case4: (60:32:8). When TL is not applied, the target domain model is trained solely based on the limited number of samples in the training set. Consequently, the average MAPE of power loss in the four cases is found to be 26.2%, 16.4%, 11.8%, and 9.9%, respectively.

During the training process for the target domain, certain adjustments are made to avoid overfitting, given the smaller number of samples available. The total number of epochs is reduced to 100, and the initial learning rate is set to 0.001. Additionally, the learning rate is halved every 20 epochs.

In each case, the training and testing processes are repeated 10 times, with the 45 experimental data randomly shuffled. The average MAPE is recorded for each testing result. The experimental results, obtained by freezing different layers, are presented in Fig. 11. The different curves represent the average

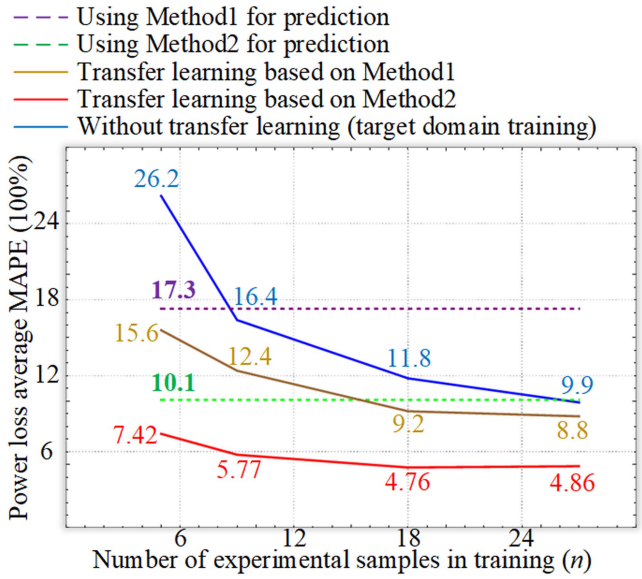

Fig. 12. Comparison between power loss evaluation using Method1 and Method2, both with and without TL refinement, and with the inclusion of target domain experimental data for training.

MAPE in different cases, considering different selections of frozen layers. In each case, the best result is indicated by a star. Remarkably, when training the target domain model with only five experimental samples, freezing all the hidden layers, and updating only the final output layer yields the best outcome. This approach achieves an average error of 7.42%, which is significantly superior to using the Method2-based source domain model for prediction (10.1% average error) or training in the target domain model (26.2% average error). As the number of experimental samples in the training process increases, the power loss average MAPE also increases. Interestingly, the minimum power loss average MAPE is achieved when freezing 1 to 4 layers. Moreover, when the ratio of training samples reaches 50%, the power loss average MAPE stabilizes, and the final minimum power loss average MAPE is around 4.8%.

A comparison between power loss evaluation using Method1 and Method2, both with and without TL refinement, and with the inclusion of target domain experimental data for training, is depicted in Fig. 12. From this comparison, several key observations can be made:

1) The incorporation of TL markedly enhances the accuracy of the target domain model in the power loss evaluation stage.
2) When dealing with limited experimental data, it is advisable to freeze all hidden layers of the target domain model. However, as more data becomes available, a gradual release of the last one or two hidden layers can be considered.
3) There is a limitation of the target domain model. Once this limit is reached, increasing the number of training samples will not yield significant improvements in precision.
4) Utilizing 45 experimental samples for power loss evaluation refinement results in a notable 50% reduction in error (from 17.3% to 9.9% based on Method1 and from 10.1% to 4.86% based on Method2). With an increase in experimental measurements, prediction error continues to decrease. This underscores that the proposed power loss evaluation refinement can consistently improve as more experiments are conducted.

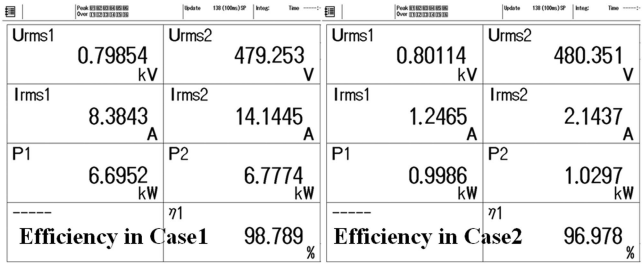

Fig. 13. Efficiency measurement results of two representative cases when $V_{\text{in}} = 480$ V, $V_{\text{o}} = 800$ V, and $f_{\text{s}} = 50$ kHz with 6.7 kW and 1.0 kW output power.

TABLE VI
KEY PARAMETERS IN TWO CASES CALCULATED IN METHOD2

Key parameters in Case1 calculated in Method2				
$I_{\text{L-AC}}$ (A)	$I_{\text{L-DC}}$ (A)	I_{S1RMS} (A)	I_{2RMS} (A)	I_{LRMS} (A)
7.689	14.889	10.220	11.285	15.226
H_{max} (AT/cm)	H_{min} (AT/cm)	B_{max} (T)	B_{min} (T)	P_{Iron} (W)
58.075	34.236	0.421	0.252	14.325
P_{Cond} (W)	P_{Copp} (W)	P_{Sw} (W)	P_{Loss} (W)	η (100%)
32.125	1.537	30.983	**78.970**	**98.835**
Key parameters in Case2 calculated in Method2				
$I_{\text{L-AC}}$ (A)	$I_{\text{L-DC}}$ (A)	I_{S1RMS} (A)	I_{2RMS} (A)	I_{LRMS} (A)
2.547	2.223	1.542	1.800	2.371
H_{max} (AT/cm)	H_{min} (AT/cm)	B_{max} (T)	B_{min} (T)	P_{Iron} (W)
10.839	2.945	0.077	0.026	7.513
P_{Cond} (W)	P_{Copp} (W)	P_{Sw} (W)	P_{Loss} (W)	η (100%)
6.333	0.229	9.794	**23.869**	**97.669**

B. Case Study on Power Loss Evaluation

This part examines two representative case studies of converter tests ($V_{\text{in}} = 480$ V, $V_{\text{o}} = 800$ V, $f_{\text{s}} = 50$ kHz with 6.7 kW, and 1.0 kW output power) to compare Method2 and the proposed power loss model. The efficiency measurements for both cases, obtained using the Yokogawa WT5000 power analyzer, are illustrated in Fig. 13. In Case 1, the power loss is $P_{\text{Loss}} = 82.2$ W with an efficiency of $\eta = 98.789\%$, while in Case 2, the power loss is $P_{\text{Loss}} = 31.1$ W with an efficiency of $\eta = 96.978\%$. The power loss calculation results for these cases, as per Method2, are summarized in Table VI.

In Case 1, where the output power is 6.7 kW, the calculated power loss error in Method2 is merely 3.93%, highlighting its suitability for high-power conditions. However, in Case 2, with a reduced output power of 1 kW, the calculated power loss error in Method2 increases to 23.25%, primarily attributed to a small power loss base value and a potential error in the calculation of P_{Iron}. In contrast, for the proposed power loss evaluation model, the predicted power loss errors in these two cases are 3.54% and 16.17% when employing 5 samples in the fine-tuning process. The errors decrease to 2.04% and 7.13% as the number of fine-tuning samples increases to 27. This underscores that the accuracy of the proposed power loss evaluation model can

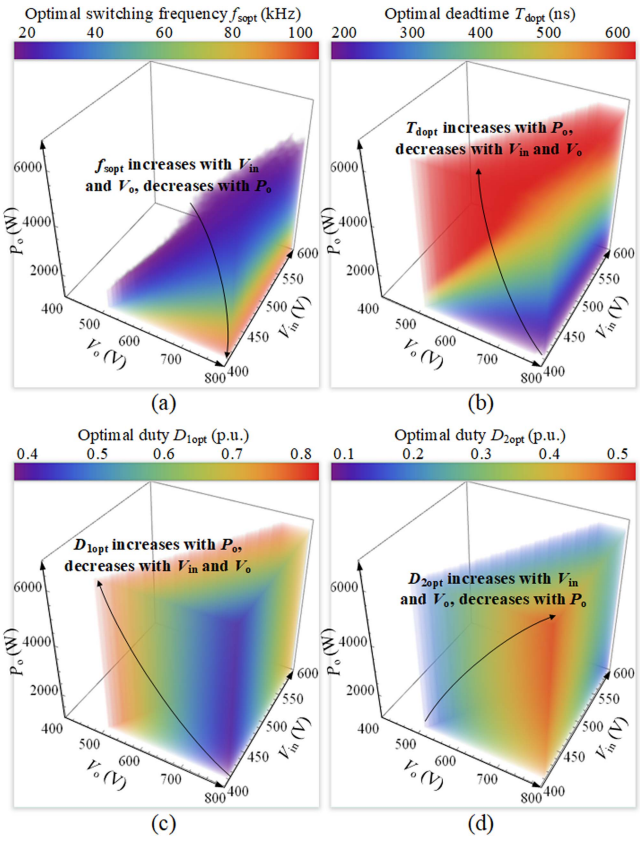

Fig. 14. Optimal control parameters for predicting the peak efficiency point using the TL refined power loss model, as determined through Method2. (a) Optimal switching frequency f_{sopt} (kHz). (b) Optimal deadtime T_{dopt} (ns). (c) Optimal duty ratio $D_{1\mathrm{opt}}$ (p.u.). (d) Optimal duty ratio $D_{2\mathrm{opt}}$ (p.u.).

be continuously enhanced with the ongoing accumulation of experimental data.

C. Peak Efficiency Searching With the Proposed Power Loss Evaluation Model

Once we acquired the refined power loss model for the TL, we determined the operation points at peak efficiency, denoted as $\eta\,(f_{\mathrm{sopt}}, T_{\mathrm{dopt}}, D_{1\mathrm{opt}}, D_{2\mathrm{opt}})$, under various input voltage V_{in}, output voltage V_{o}, and output power P_{o} conditions. These results are illustrated in Fig. 14. During the peak efficiency search phase, we specified the following ranges for V_{in}, V_{o}, and P_{o}: 400 V $\leq V_{\mathrm{in}} \leq$ 600 V, $1.2\times V_{\mathrm{in}} \leq V_{\mathrm{o}} \leq$ 800 V, 1 kW $\leq P_{\mathrm{o}} \leq$ 6.6 kW. We explored switching frequencies ranging from 20 to 100 kHz. It is worth noting that f_{sopt} and $D_{2\mathrm{opt}}$ increase as V_{in} and V_{o} increase but decrease as P_{o} increases. Conversely, T_{dopt} and $D_{1\mathrm{opt}}$ increase as P_{o} increases, but decrease as V_{in} and V_{o} increase. Since the voltage gain of the converter is primarily determined by D_1 and D_2, the changes in $D_{1\mathrm{opt}}$ and $D_{2\mathrm{opt}}$ are relatively small under different output power conditions.

It is crucial to emphasize the significance of determining individual power loss components during the experimental verification phase. This process allows us to gain insights into the breakdown of power losses and their distribution across various electrical components. However, it is currently challenging for us to tackle this issue effectively. The primary obstacle lies in our difficulty in accurately measuring the power losses of each electrical component in our experiments. Essentially, we lack the ground truth data for P_{Cond}, P_{Copp}, P_{Iron}, P_{ON}, and P_{OFF} for each experimental sample. From an ANN perspective, this problem falls under the category of "unsupervised learning." Since the experimental data lack labels, ANNs struggle to adjust the weights and biases of their neurons to minimize the disparity between predictions and actual values.

TABLE VII
COMPARISON BETWEEN THE PROPOSED METHOD AND CONVENTIONAL METHODS

	Proposed model	Conventional model
Accuracy	Achieving high accuracy across the entire range of conditions.	Moderate in high-power conditions, and low in low-power conditions.
Adaptability	Self-adaptive, accuracy improves with ongoing of experimental data.	Nonadaptive, fixed evaluation error in average power loss assessment
Guidance on peak efficiency searching	Facilitate the search for the peak efficiency point and the corresponding control parameters.	Suitable for searching the peak efficiency point but often yields nonoptimal control parameters.
Model complexity	1) Time-consuming during the data acquisition process due to iterative simulations* 2) User-friendly when the model is finely tuned.	1) Time-saving for acquiring a simplified yet inaccurate power loss model. Time-consuming when involved with iterative simulations. 2) Convenient to use once the model is obtained.

* In Method2, the acquisition of 233,280 samples takes 14.5 days, attributed to extensive iterative simulations. Conversely, Method1 expedites this process by solely employing an analytical method for sample generation. However, the average MAPE of power loss prediction reduces from 17.3% to 10.1%.

To align the accumulation of total power loss with the predictions of the refined TL power loss model, we apply a constant coefficient to each component: P_{Cond}, P_{Copp}, P_{Iron}, P_{ON}, and P_{OFF}. Fig. 15 illustrates both the peak efficiency η_{Peak} and the minimum values of each power loss component, represented as P_{Condmin}, P_{Coppmin}, P_{Ironmin}, P_{ONmin}, and P_{OFFmin}.

The maximum peak efficiency, max(η_{Peak}) is attained at V_{in} = 590 V, V_{o} = 708 V, and P_{o} = 6.6 kW. With a small voltage difference ($V_{\mathrm{o}} - V_{\mathrm{in}}$), minimal ripple current, and a high-power base value, the maximum efficiency reaches 99.43%.

Conversely, the minimum peak efficiency, min(η_{Peak}) = 96.23% occurs when V_{in} = 400 V,V_{o} = 800 V, P_{o} = 1 kW. The maximum values of P_{Condmin}, P_{Coppmin}, and P_{OFFmin} are all achieved when V_{in} = 400 V, V_{o} = 800 V, P_{o} = 6.6 kW. In this operating condition, both the current ripple and turn-OFF current reach their maximum levels. P_{Ironmin} remains high when V_{in} = 400 V, V_{o} = 800 V, and its relationship with P_{o} is not obvious. The maximum value for P_{ONmin} is reached when V_{in} = 400 V, V_{o} = 480 V, P_{o} = 6.6 kW, primarily due to the peak turn-ON current in the hard-switching condition. In typical operating regions where $V_{\mathrm{o}} - V_{\mathrm{in}}$ and P_{o} are both small, both power MOSFETs achieve ZVS-ON, resulting in P_{ON} being zero in this region.

In conclusion, Table VII presents a comparison between the proposed power loss evaluation model and conventional models. The proposed method is characterized by its data-driven nature,

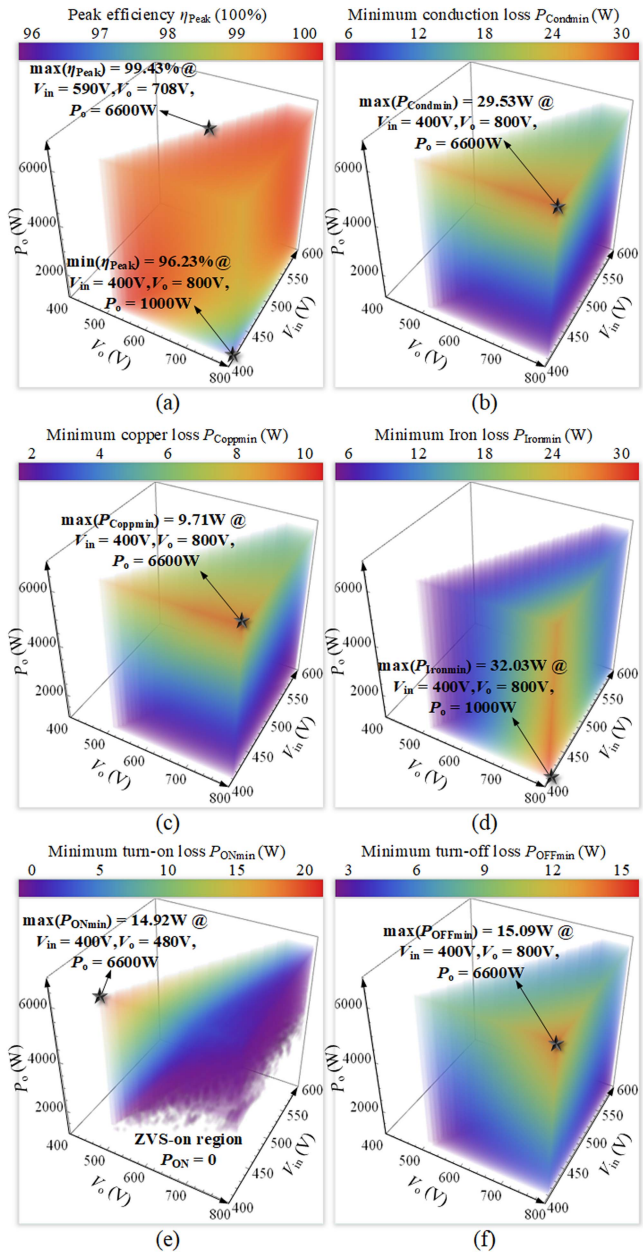

Fig. 15. Prediction of efficiency and power loss breakdown using the TL refined power loss model, as determined through Method2. (a) Peak efficiency η_{Peak} (100%). (b) Minimum conduction loss P_{Condmin} (W). (c) Minimum copper loss P_{Coppmin} (W). (d) Minimum Iron loss P_{Ironmin} (W). (e) Minimum turn-ON loss P_{ONmin} (W). (f) Minimum turn-OFF loss P_{OFFmin} (W).

self-adaptability, and its ability to streamline the search for the peak efficiency point along with the corresponding control parameters. Despite the time-consuming process of acquiring a large-scale, high-quality dataset through extensive iterative simulations, the model remains user-friendly once the power loss evaluation model is fine-tuned.

V. Conclusion

A precise evaluation of power converter losses is essential for accurately predicting power loss and optimizing control parameters to enhance efficiency across various scenarios and applications. This article introduces a TL-based refinement approach for power loss evaluation, which can be continuously enhanced with ongoing experimental data. Our method involves the creation of a comprehensive source domain dataset for training a source domain model, followed by fine-tuning in the target domain. As an illustrative example, we consider a 6.6 kW synchronous boost converter, accounting for six degrees of freedom in operational conditions. Leveraging a dataset comprising 2 33 280 samples from simulations and 45 samples from experiments, our refined power loss evaluation model achieved a remarkable 50% reduction in average power loss error compared with conventional methodologies. With the guidance of the TL refined power loss model, we can determine the peak efficiency and the corresponding optimal control parameters.

References

[1] M. İnci et al., "A review and research on fuel cell electric vehicles: Topologies, power electronic converters, energy management methods, technical challenges, marketing and future aspects," *Renewable Sustain. Energy Rev.*, vol. 137, 2021, Art. no. 110648.

[2] J. M. Carrasco et al., "Power-electronic systems for the grid integration of renewable energy sources: A survey," *IEEE Trans. Ind. Electron.*, vol. 53, no. 4, pp. 1002–1016, Jun. 2006.

[3] F. Blaabjerg, Z. Chen, and S. B. Kjaer, "Power electronics as efficient interface in dispersed power generation systems," *IEEE Trans. Power Electron.*, vol. 19, no. 5, pp. 1184–1194, Sep. 2004.

[4] K. Sun, L. Zhang, Y. Xing, and J. M. Guerrero, "A distributed control strategy based on DC bus signaling for modular photovoltaic generation systems with battery energy storage," *IEEE Trans. Power Electron.*, vol. 26, no. 10, pp. 3032–3045, Oct. 2011.

[5] A. Y. Saber and G. K. Venayagamoorthy, "Plug-in vehicles and renewable energy sources for cost and emission reductions," *IEEE Trans. Ind. Electron.*, vol. 58, no. 4, pp. 1229–1238, Apr. 2011.

[6] R. Tavakoli and Z. Pantic, "Analysis, design, and demonstration of a 25-kW dynamic wireless charging system for roadway electric vehicles," *IEEE J. Emerg. Sel. Topics Power Electron.*, vol. 6, no. 3, pp. 1378–1393, Sep. 2018.

[7] A. Poorfakhraei, M. Narimani, and A. Emadi, "A review of multilevel inverter topologies in electric vehicles: Current status and future trends," *IEEE Open J. Power Electron.*, vol. 2, pp. 155–170, 2021.

[8] A. Q. Huang, M. L. Crow, G. T. Heydt, J. P. Zheng, and S. J. Dale, "The future renewable electric energy delivery and management (FREEDM) system: The energy internet," *Proc. IEEE*, vol. 99, no. 1, pp. 133–148, Jan. 2011.

[9] H. Kanchev, D. Lu, F. Colas, V. Lazarov, and B. Francois, "Energy management and operational planning of a microgrid with a PV-based active generator for smart grid applications," *IEEE Trans. Ind. Electron.*, vol. 58, no. 10, pp. 4583–4592, Oct. 2011.

[10] X. Wang and F. Blaabjerg, "Harmonic stability in power electronic-based power systems: Concept, modeling, and analysis," *IEEE Trans. Smart Grid*, vol. 10, no. 3, pp. 2858–2870, May 2019.

[11] M. H. Ahmed, C. Fei, F. C. Lee, and Q. Li, "48-V voltage regulator module with PCB winding matrix transformer for future data centers," *IEEE Trans. Ind. Electron.*, vol. 64, no. 12, pp. 9302–9310, Dec. 2017.

[12] M. Kasper, D. Bortis, G. Deboy, and J. W. Kolar, "Design of a highly efficient (97.7%) and very compact (2.2 kW/dm^3) isolated AC–DC telecom power supply module based on the multicell ISOP converter approach," *IEEE Trans. Power Electron.*, vol. 32, no. 10, pp. 7750–7769, Oct. 2017.

[13] Z. Ye, Y. Lei, and R. C. N. Pilawa-Podgurski, "The cascaded resonant converter: A hybrid switched-capacitor topology with high power density and efficiency," *IEEE Trans. Power Electron.*, vol. 35, no. 5, pp. 4946–4958, May 2020.

[14] H. Akagi, T. Yamagishi, N. M. L. Tan, S. Kinouchi, Y. Miyazaki, and M. Koyama, "Power-loss breakdown of a 750-V 100-kW 20-kHz bidirectional isolated DC–DC converter using SiC-MOSFET/SBD dual modules," *IEEE Trans. Ind. Appl.*, vol. 51, no. 1, pp. 420–428, Jan./Feb. 2015.

[15] M. Leibl, G. Ortiz, and J. W. Kolar, "Design and experimental analysis of a medium-frequency transformer for solid-state transformer applications," *IEEE J. Emerg. Sel. Topics Power Electron.*, vol. 5, no. 1, pp. 110–123, Mar. 2017.

[16] G. Ortiz, M. G. Leibl, J. E. Huber, and J. W. Kolar, "Design and experimental testing of a resonant DC–DC converter for solid-state transformers," *IEEE Trans. Power Electron.*, vol. 32, no. 10, pp. 7534–7542, Oct. 2017.
[17] J. Muhlethaler, J. Biela, J. W. Kolar, and A. Ecklebe, "Improved core-loss calculation for magnetic components employed in power electronic systems," *IEEE Trans. Power Electron.*, vol. 27, no. 2, pp. 964–973, Feb. 2012.
[18] J. Muhlethaler, J. Biela, J. W. Kolar, and A. Ecklebe, "Core losses under the DC bias condition based on Steinmetz parameters," *IEEE Trans. Power Electron.*, vol. 27, no. 2, pp. 953–963, Feb. 2012.
[19] D. Serrano et al., "Why magnet: Quantifying the complexity of modeling power magnetic material characteristics," *IEEE Trans. Power Electron.*, vol. 38, no. 11, pp. 14292–14316, Nov. 2023.
[20] F. Zámborszky, D. Tóth, Z. Palánki, and E. Csizmadia, "Electrical and calorimetric power loss measurements of practically ideal soft magnetic cores," *IEEE Trans. Magn.*, vol. 50, no. 4, Apr. 2014, Art. no. 6300604.
[21] P. Papamanolis, T. Guillod, F. Krismer, and J. W. Kolar, "Transient calorimetric measurement of ferrite core losses up to 50 MHz," *IEEE Trans. Power Electron.*, vol. 36, no. 3, pp. 2548–2563, Mar. 2021.
[22] M. Kasper, R. M. Burkart, G. Deboy, and J. W. Kolar, "ZVS of power MOSFETs revisited," *IEEE Trans. Power Electron.*, vol. 31, no. 12, pp. 8063–8067, Dec. 2016.
[23] R. Li, X. Wu, S. Yang, and K. Sheng, "Dynamic on-state resistance test and evaluation of GaN power devices under hard- and soft-switching conditions by double and multiple pulses," *IEEE Trans. Power Electron.*, vol. 34, no. 2, pp. 1044–1053, Feb. 2019.
[24] Y. Yan, H. Gui, and H. Bai, "Complete ZVS analysis in dual active bridge," *IEEE Trans. Power Electron.*, vol. 36, no. 2, pp. 1247–1252, Feb. 2021.
[25] S. J. Pan and Q. Yang, "A survey on transfer learning," *IEEE Trans. Knowl. Data Eng.*, vol. 22, no. 10, pp. 1345–1359, Oct. 2010.
[26] K. He et al., "Deep residual learning for image recognition," in *Proc. IEEE Conf. Comput. Vis. Pattern Recognit.*, 2016, pp. 770–778.
[27] J. Redmon et al., "You only look once: Unified, real-time object detection," in *Proc. IEEE Conf. Comput. Vis. Pattern Recognit.*, 2016, pp. 779–788.
[28] A. Radford, K. Narasimhan, T. Salimans, and I. Sutskever, "Improving language understanding by generative pre-training," 2018.
[29] J. Devlin et al., "Bert: Pre-training of deep bidirectional transformers for language understanding," 2018, *arXiv:1810.04805*.

Ziheng Xiao (Member, IEEE) received the B.S. degree in electrical engineering and automation and Ph.D. degree in electrical engineering from the College of Electrical and Information Engineering, Hunan University, Changsha, China, in 2017 and 2022, respectively.

Since 2022, he has been a Research Fellow with Energy Research Institute, Nanyang Technological University, Singapore. His main research interests include the medium voltage dc system, dual active bridge converters, resonant converters, energy router, and the application of artificial intelligence in power electronics.

Dr. Xiao was the Session Chair for the 49th Annual Conference of IEEE Industrial Electronics Society (IES).

Yu Jiang (Member, IEEE) received the B.S. degree in electrical engineering and automation and Ph.D. degree in control theory and control engineering from the College of Electrical and Information Engineering, Hunan University, Changsha, China, in 2017 and 2023, respectively.

Since 2023, she has been a Research Fellow with The Chinese University of Hong Kong, Hong Kong. Her research interests include nonlinear analysis, chaos theory, pattern recognition, and machine learning for industrial process applications.

Tengfei Sun (Graduate Student Member, IEEE) received the B.S. degree in electrical engineering and automation from Guangzhou University, Guangzhou, China, in 2017, and the M.S. degree in power electronics and power drives from Beijing Institute of Technology, Beijing, China, in 2020. He is currently working toward the Ph.D. degree in electrical engineering with Nanyang Technological University, Singapore.

His research interests include the modulation and control of power converters, and high-frequency power conversion.

Yue Wu (Graduate Student Member, IEEE) received the B.S. degree in electrical engineering and automation in 2018 from the School of Electrical Engineering, Xi'an Jiaotong University, Xi'an, China, where he is currently working toward the Ph.D. degree in electrical engineering.

Since 2022, he has been working as a jointly supervised Ph.D. student with the School of Electrical and Electronic Engineering, Nanyang Technological University, Singapore. His main research interests include wireless power transfer, design and optimization of resonant coils, and the resonant coil modeling.

Yi Tang (Senior Member, IEEE) received the B.Eng. degree in electrical engineering from Wuhan University, Wuhan, China, in 2007, and the M.Sc. degree in power electronics and power drives and Ph.D. degree in electrical engineering from the School of Electrical and Electronic Engineering, Nanyang Technological University, Singapore, in 2008 and 2011, respectively.

From 2011 to 2013, he was a Senior Application Engineer with Infineon Technologies Asia Pacific, Singapore. From 2013 to 2015, he was a Postdoctoral Research Fellow with Aalborg University, Aalborg, Denmark. Since March 2015, he has been with Nanyang Technological University, where he is currently a tenured Associate Professor. His research interests include power electronics and its applications in smart grid and e-mobility systems.

Dr. Tang was the recipient of the Infineon Top Inventor Award in 2012, the Early Career Teaching Excellence Award in 2017, and four IEEE Prize Paper Awards. He serves as an Associate Editor for IEEE TRANSACTIONS ON POWER ELECTRONICS (TPEL) and IEEE JOURNAL OF EMERGING AND SELECTED TOPICS IN POWER ELECTRONICS (JESTPE).